Available online at www.sciencedirect.com

ScienceDirect

Procedia CIRP 31 (2015) 1 – 6

www.elsevier.com/locate/procedia

15th CIRP Conference on Modelling of Machining Operations

Surface Layer Modification by Cryogenic Burnishing of *Al 7050-T7451* Alloy and Validation with FEM-Based Burnishing Model

B. Huang[a]*, Y. Kaynak[b], Y. Sun[a], I.S. Jawahir[a]

[a]Department of Mechanical Engineering, and Institute for Sustainable Manufacturing (ISM), University of Kentucky, Lexington, KY 40506, USA
[b]Department of Mechanical Engineering, Faculty of Technology, Marmara University, Goztepe Campus, Kadikoy, 34722, Istanbul, Turkey
* Corresponding author. Tel.: +1 859 323 3256; *E-mail address*: bo.huang@uky.edu

Abstract

As one of the chipless machining processes, burnishing has been performed on manufactured components as the final operation to improve the surface integrity, including reduced surface roughness and increased surface and subsurface hardness. Refined surface layers with ultra-fine grains or nano-grains could be generated during the burnishing process due to imposed severe plastic deformation and the associated dynamic recrystallization (DRX). These harder layers with compressive residual stresses induced by the burnishing process also provide added benefits by enhancing wear/corrosion resistance and increasing the fatigue life of the components. The research findings presented in this paper show the effects of cryogenic burnishing with roller burnishing tool on *Al 7050-T7451* alloy, using liquid nitrogen as the coolant. Burnishing forces and temperatures are measured to compare the differences between dry and cryogenic burnishing. Higher tangential forces and lower temperatures are observed from cryogenic burnishing due to the work-hardening and the rapid cooling effects introduced by cryogenic burnishing. Also, refined layers with nano-grains (grain size of approximately 40 nm) are formed in the cryogenically burnished surface, in which an average hardness increase of 9.5%, 17.5% and 24.8% within the 200 µm depth are achieved in comparison with the hardness values obtained from dry burnishing, at the corresponding burnishing speeds of 25, 50 and 100 m/min. A finite element model (FEM) is developed to simulate the burnishing forces and temperatures for validation of the experimental results, based on the modified Johnson-Cook flow stress model combined with the constitutive equations concerning DRX. Good agreement is obtained between the predicted and experimental results.

Peer-review under responsibility of the International Scientific Committee of the "15th Conference on Modelling of Machining Operations

Keywords: Cryogenic burnishing; Nano structure; Hardness; FEM.

1. Introduction

Severe plastic deformation (SPD) processes have been regarded as the effective methods to introduce exceptional grain refinement in the metallic work materials without changing their overall dimensions significantly [1]. The typical SPD processes include equal channel angular pressing (ECAP), high-pressure torsion (HPT), accumulative roll bonding (ARB), etc. To apply these processes, the desired material properties could be achieved by controlling the grain size which is the critical microstructural factor influencing the mechanical behavior of the metallic work materials and their chemical response to the surrounding environments [2]. Burnishing is a SPD process to induce high strain and strain-rate [3] for the purpose of improving the surface integrity of the manufactured components. Grzesik and Zak [4] reported that lower surface roughness was obtained by ball burnishing of *41Cr4* low-alloy steel with 60 HRC hardness. Klocke et al. [5] showed property improvement in turbine blades made of Inconel *718* and *Ti-6Al-4V* were symmetrically burnished by two roller burnishing tools working simultaneously from both sides to avoid plastic component deflection, low fatigue life due to the effect of strain hardening and the compressive residual stress induced by the burnishing process. Low plasticity burnishing (LPB) increased the corrosion fatigue strength of *Al 7075-T6* alloy to 310 MPa, which was three times compared with the unburnished samples according to the research conducted by Prevey and Cammett [6].

Cryogenic burnishing, with liquid nitrogen as the coolant during the burnishing process, is capable of generating refined surface layers with nano or ultra-fined grains as the heat generated during burnishing is taken away quickly and the grain growth of the recrystallized grains in the burnished surface and sub-surface is constrained after dynamic

Peer-review under responsibility of the International Scientific Committee of the "15th Conference on Modelling of Machining Operations
doi:10.1016/j.procir.2015.03.097

recrystallization (DRX). These refined surface layers with higher hardness and compressive residual stress due to the mechanism of SPD and grain refinement, would provide benefits to enhance the mechanical and physical properties of the components, such as improving their corrosion/wear resistance and increasing their fatigue lives. Pu et al. [7] found that ultra-fine grained surface layer was formed in the burnished surface of *AZ31B Mg* alloy, in which the surface hardness was increased from 0.86 to 1.35 GPa and the corrosion resistance was significantly improved due to the grain refinement associated with the strong basal texture induced by cryogenic burnishing. Similar observation was made in the study of cryogenic burnishing of *Co-Cr-Mo* biomedical alloy by Yang et al. [8]. Microstructure refinement was achieved in the burnished surface where grains of 300-600 nm size were distributed in the refined surface layers with 87% increased hardness compared to the bulk materials. The improved wear performance of this biomedical material was attributed to the cryogenic burnishing-induced surface integrity enhancement [9].

Al 7050-T7451 alloy has good properties including strength, toughness and crack resistance that make it the premier selection for the plate applications, such as the fuselage frames, bulkheads, wing skins, etc. [10]. However, its mechanical and material properties need to be improved to broaden its applications. In this study, friction stir processing (FSP) is used to process the as-received materials to achieve the ultra-fine grained (UFG) structure as the first step, and then cryogenic burnishing is performed to introduce further microstructure refinement on the burnished surface to obtain the refined surface layer with nano-grains in which the hardness in this layer can be increased, while the corrosion/wear resistance could be improved.

2. Experimental Work

The work material used in the experiments was *Al 7050-T7451* alloy with UFG structure produced by FSP, initially a plate/sheet with 3.22 mm thickness was processed by double-sided FSP. The rotational speed of the FSP tool was 19.2 m/min and the feed rate was 101.6 mm/min. The sheet was cut into discs with 65 mm diameter by vertical milling. The average grain size of the processed disc after FSP was approximately 1.82 μm. Each disc was fixed on a specially-designed work-holding mandrel using three bolts and orthogonal burnishing was performed on a *HAAS TL-2 CNC* lathe. Fig. 1 illustrates the experimental setup for cryogenic burnishing of UFG *Al 7050-T7451* disc.

A roller burnishing tool made of uncoated carbide with the diameter of 14.3 mm was used in the burnishing experiments, and the roller head was not fixed and could rotate along with the disc during burnishing. Depth of penetration was selected as 0.2 mm while the burnishing speeds used in the dry and cryogenic burnishing experiments were 25, 50 and 100 m/min. The dwell time between the burnishing tool and the disc was set to be 10 seconds after the depth of penetration was achieved.

A Kistler *9121* three-component tool dynamometer was used to measure the radial and tangential force components during dry and cryogenic burnishing experiments. Liquid nitrogen was delivered from the clearance side of the burnishing tool by ICEFLY® system, and the flow rate was approximately *10g/s* mass under 1.5MPa pressure. FLIR infrared camera was used to measure the temperature of *Al 7050-T7451* discs in dry and cryogenic burnishing. For the purpose of studying the surface integrity aspects, the metallurgical samples were cut from the burnished discs. In the sequential order, a range of metallurgical operations such as mounting, grinding, polishing and etching were performed to reveal the microstructure of the samples. Keller's reagent was used to etch the samples of *Al 7050-T7451* alloy.

To observe the microstructure, Nikon EPIPHOT 300 with Leica DFC425 optical microscope was used in the experiments. Atomic force microscopy (AFM) images were taken by Agilent Technologies 5500 Scanning Probe Microscope to observe the nano-grains generated in the refined surface layers from cryogenic burnishing. Hardness was measured using one Vickers indenter of the CSM Micro-Combi Tester in which 25 gf load and 15 seconds duration were selected to make the indentation.

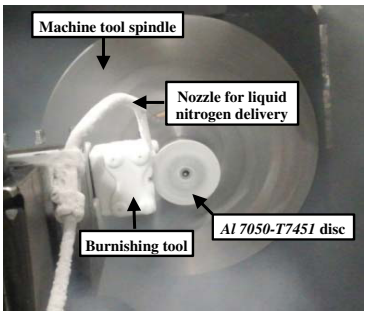

Fig. 1. Experimental setup for cryogenic burnishing.

3. Results and Discussion

3.1. Burnishing forces

Two force components (tangential and radial) were measured in the burnishing experiments under dry and cryogenic circumstances. As shown in Fig. 2, for dry burnishing, a decreasing trend could be observed from both the radial and tangential forces as the burnishing speed increased. The distribution of the burnishing temperatures corresponding to each burnishing speed is presented later in Fig. 6 which is very helpful to explain this phenomenon. When the temperature increases due to higher burnishing speed, the material becomes softer and the thermal softening effect is more dominant that leads to reduced yield stress of *Al 7050-T7451* alloy at higher temperature.

However, in the case of cryogenic burnishing, the radial force components are relatively stable as the heat generated during burnishing is taken away by liquid nitrogen in a very short time and the thermal conductivity of *Al 7050-T7451 alloy* is very high, thus the heat will not build up and accumulate during cryogenic burnishing and the thermal softening effect will not play an important role in cryogenic burnishing. Due to the cooling effect with liquid nitrogen, the material becomes harder and stronger and the resulting higher

yield stress [11] makes the material more difficult to be burnished compared with dry burnishing. This explains why the tangential forces of cryogenic burnishing are higher than in dry burnishing. Similar experimental results were also found in the work of Yang et al. [12].

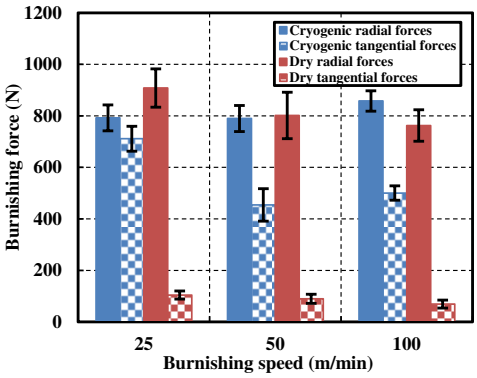

Fig. 2. Radial and tangential forces measured from dry and cryogenic burnishing (the depth of penetration is 0.2 mm, the burnishing speeds are 25, 50 and 100 m/min).

3.2. FEM model and simulation results

A numerical model was developed based on the commercial FEM software DEFORM-2D™ with a Lagrangian implicit code, to simulate dry and cryogenic burnishing of *Al 7050-T7451* alloy in terms of radial force components and temperatures. The workpiece mesh element number was set at 8000 while the tool was meshed with 3000 isoparametric quadrilateral elements. In addition, a finer mesh window is kept near the tool-workpiece contact area in order to obtain a deeper insight into the results due to the large deformation occurring there. For the details of the model development, the inter-object boundary conditions between the tool and workpiece are assumed to be shear friction type, where the friction coefficient is considered to be 0.38 through the calibration with the experimental force data in which the minimum error could be achieved between the simulated and experimental results, while the heat capacity and the specific heat capacity are determined depending on the simulation calibration and literature research [13]. An environmental window is maintained behind the tool to simulate the cooling effect of liquid nitrogen whose size is approximately 3mm ×1mm. In the heat exchange window, the local temperature is -184 ºC and the convection coefficient of the local heat exchange is 10000 kW/(m^{2}K) [9]. The details of the numerical model are illustrated in Fig. 3.

Dynamic recrystallization was taken into consideration in order to achieve more accurate simulation results. Before DRX occurs when the critical strain is not reached, the governing flow stress equation used in the study is Johnson-Cook material model [14]. After the critical strain is reached, the constitutive equations, characterizing the flow stress behaviour after DRX, are borrowed from the study of Wu et al. [15] to reflect the effects of microstructure change on the flow stress, based on their experimental results and kinetic analysis. A specific user-subroutine has been programmed to apply the flow stress model used in this study by combining Johnson-Cook governing before DRX and the constitutive equations governing after DRX. Fig. 4 illustrates the dynamic recovery curve relates to the flow stress without considering DRX while the dynamic recrystallization curve corresponds to the flow stress considering DRX [16]. Eqn. (1) is Johnson-Cook flow stress equation and Eqns. (2) to (10) show the constitutive equations describing the flow stress after DRX occurs [15]. Radial force components and temperatures are simulated to compare the predicted results with the experimental data.

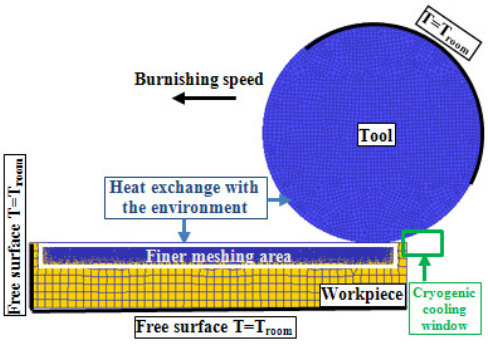

Fig. 3. The boundary conditions of FEM numerical model for cryogenic burnishing.

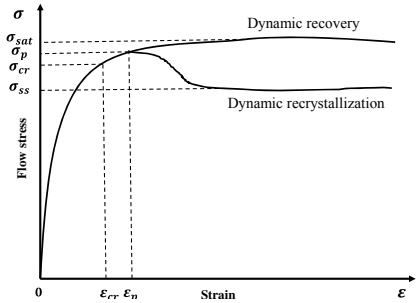

$$\sigma_{DRV} = (A + B\,\varepsilon^{n})(1 + C\ln\dot{\varepsilon})[1 - \left(\frac{t - t_r}{t_m - t_r}\right)^{m}] \quad (\varepsilon < \varepsilon_{cr}) \tag{1}$$

$$\sigma_{DRX} = \sigma_{DRV} - (\sigma_{sat} - \sigma_{ss})\left\{1 - \exp(-K\left(\frac{\varepsilon - \varepsilon_{cr}}{\varepsilon_p}\right)^{1.39}\right\} \quad (\varepsilon \geq \varepsilon_{cr}) \tag{2}$$

$$\sigma_{sat} = 66.4 sinh^{-1}[\left(\frac{Z}{6.23\times10^{7}}\right)^{0.2}] \tag{3}$$

$$\sigma_{ss} = 66.4 sinh^{-1}\left\{[\frac{\dot{\varepsilon}\exp(136836/(R(T+\Delta T)))}{2.07\times10^{9}}]^{0.21}\right\} \tag{4}$$

$$Z = \dot{\varepsilon}\exp(\frac{122132}{RT}) \tag{5}$$

$$\Delta T = 1.30\,Z^{0.14}\,\eta \tag{6}$$

$$\eta = \begin{cases} 1 & (\dot{\varepsilon} \geq 1.0) \\ \frac{1}{3}(3 + \ln(\dot{\varepsilon})) & (10^{-3} < \dot{\varepsilon} < 1.0) \\ 0 & (\dot{\varepsilon} \leq 10^{-3}) \end{cases} \tag{7}$$

$$K = 5.02 \times 10^{-3}\,Z^{0.13} \tag{8}$$

$$\varepsilon_p = 1.07 \times 10^{-3}\,Z^{0.19} \tag{9}$$

$$\varepsilon_{cr} = 8.54 \times 10^{-4}\,Z^{0.19} \tag{10}$$

In Eqns. (1) and (2), σ_{DRV} is the equivalent flow stress of dynamic recovery; The constant A and B represent the initial yield strength and hardness modulus of the material respectively; C is the strain-rate sensitivity coefficient; ε is the equivalent strain and $\dot{\varepsilon}$ is the effective strain rate; n and m represent the hardening coefficient and the thermal softening exponent; t, t_m and t_r are the temperature of the workpiece, the material melting temperature and the reference room

temperature; σ_{DRV} and σ_{DRX} refer to the equivalent flow stresses before and after DRX occurs; σ_{sat} and σ_{ss} are the saturation flow stress without considering DRX and the steady flow stress after DRX occurs; K is the material constant based on the deformation condition; ε_{cr} is the critical strain determining when DRX occurs and ε_p are the peak strain; Z represents Zener-Hollomon parameter where R is the universal gas constant; ΔT and η are the temperature rise and the heat conversion factor.

To determine the material constants of *Al 7050-T7451* alloy, calibrations have been made with the curve fitting between the calculated the flow stress and the flow stress data provided by Wu et al. [15]. Through the calibration, A and B has been determined to be 420 and 30 MPa. Learning from the work of Wang et al. [17], Wang et al. [18] and Fu et al. [19], the values of C, n, m, t_m and t_r are 0.005, 0.32, 0.99, 635 and 20 respectively while Eqns. (2) to (10) were borrowed from Wu et al. [15]. By observing the differences of temperatures and radial forces from Figs. 5 and 6, good agreements are obtained between the simulated and experimental results. The differences between the predicted and experimental results are listed above the bars representing the simulated values. Less than 10% of percentage differences is achieved for most of the radial forces prediction, however there are some variations for the highest burnishing temperatures especially in the case of low burnishing speeds, further modifications of the theory would be needed in order to the make the model more accurate.

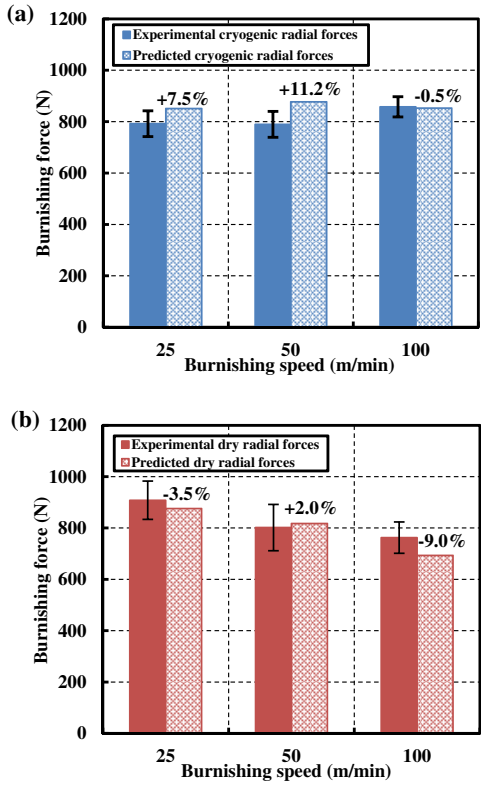

Fig. 5. The comparison between predicted and experimental results: (a) cryogenic burnishing radial forces and (b) dry burnishing radial forces (the depth of penetration is 0.2 mm, the burnishing speeds are 25, 50 and 100 m/min).

3.3. Burnishing temperatures

For obtaining more accurate temperature measurements, the emissivity of the *Al 7050-T7451* alloy disc used in the burnishing experiments is determined by researching the previous work from the literature review since it is one of the most important factors influencing the accuracy of infrared camera. The emissivity of *Al 7050* and *Al 7075* alloys are considered to be options for the setup of infrared camera as they are both of *7xxx* series aluminum alloys and have similar material properties. The range within 0.05 to 0.2 was found to be reasonable for these two aluminum alloys [20, 21, 22], and through the calibration and comparison with the similar temperature measurements for machining of *Al 7050* alloy [19, 22, 23, 24], 0.09 is used as the emissivity in this study.

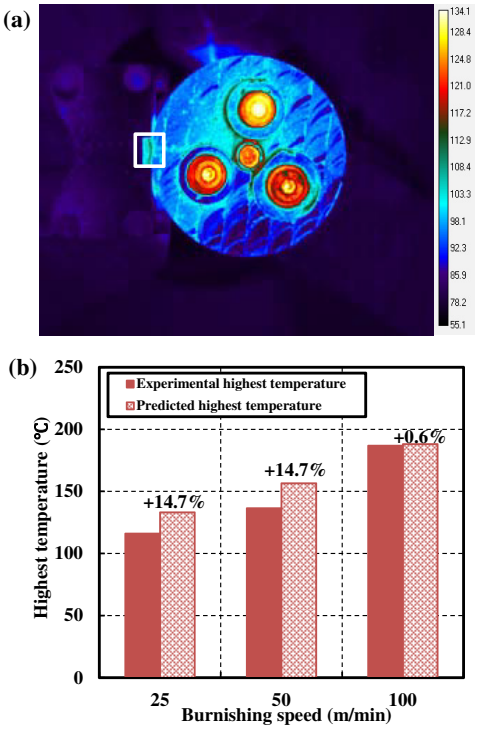

Fig. 6 (a) The infrared image of temperature measurement (dry burnishing at depth of penetration of 0.2 mm and burnishing speed of 25 m/min); (b) The highest temperatures measured in the dry burnishing areas at three different burnishing speeds and the corresponding simulation results.

As shown in Fig. 6 (a), the white rectangular section represents the area where the highest temperature is measured in the contact zone between the burnishing tool and the workpiece during dry burnishing. In cryogenic burnishing, the temperature cannot be measured as the heat generated by burnishing is taken away by liquid nitrogen in a relatively short time which is beyond the capability of the infrared camera to record the temperature below zero degree. Fig. 6 (b) shows an increasing trend when increasing the burnishing speed. Since more heat would build up in the tool-workpiece contact area in the same dwelling time around 10 seconds after the depth of penetration was reached, the temperature is higher at higher speeds. These findings are consistent with the study of Yang [9].

3.4. Microstructure

A strong microstructure change was observed in cryogenic burnishing, where a refined layer was formed in the burnished subsurface. This apparent refined layer with a featureless characteristics and the subsequent transition layer with the pattern of sweeping grains existed in the burnished surface and sub-surface under the cryogenic conditions at three different burnishing speeds as shown in Fig. 7. Nano-grains with the grain size of 38.9±3.3 nm (95% confidence level) as shown in Fig. 7 (a), were observed in the AFM image taken from the refined layer at the depth of penetration of 0.2 mm and burnishing speed of 25 m/min.

The average measured values of refined layer depth are 52.1, 44.9 and 24.2 μm respectively when the burnishing speeds are 25, 50 and 100 m/min. The reason for this is that the grain growth is supressed the most as the cooling effect of liquid nitrogen plays more important role when the burnishing speed is low. The highest temperatures measured by the infrared camera as shown in Fig. 6, indicated that more heat was accumulated at high burnishing speed in dry burnishing. Similar heat would build up in cryogenic burnishing, and it would take more time for liquid nitrogen to take the heat away at high burnishing speed, compared with the case at low burnishing speed. In the meantime, the recrystallized grains have more time to grow. Therefore, the depth of refined layers becomes smaller as the recrystallized grains in the subsurface will grow larger at higher burnishing speeds. However, no microstructure change was observed in the burnished surface and subsurface from dry burnishing due to the grain growth after DRX occurs without any cooling effect.

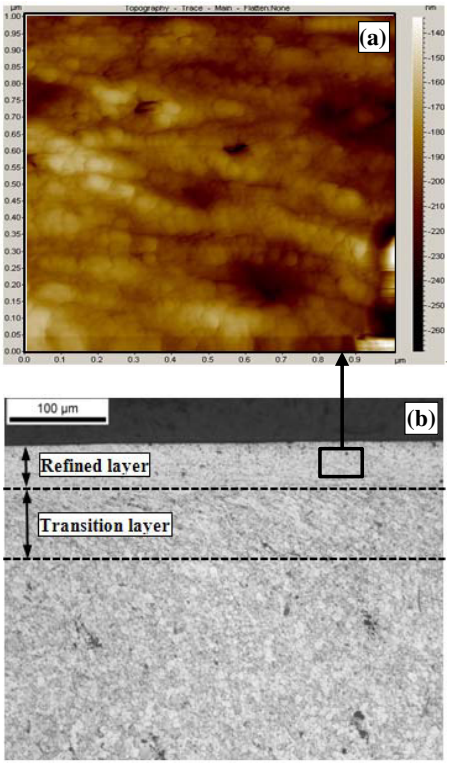

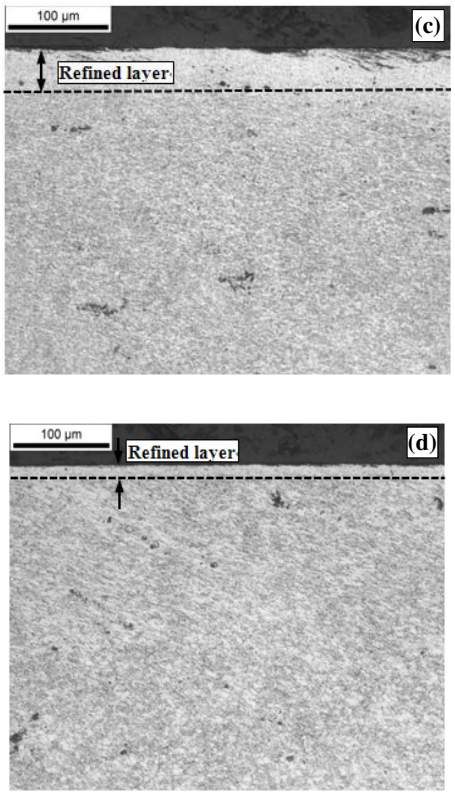

Fig. 7. The microstructure of *Al 7050-T7451* alloy from cryogenic burnishing at the depth of penetration of 0.2 mm: (a) AFM image (at the burnishing speed of 25 m/min); (b) microstructure at the burnishing speed of 25 m/min; (c) microstructure at the burnishing speed of 50 m/min; (d) microstructure at the burnishing speed of 100 m/min.

3.5. Hardness

The hardness was measured in the burnished surface and subsurface for dry and cryogenic burnishing at the three different burnishing speeds. Fig. 8 shows that, the surface hardness of all the three cryogenic burnishing samples is all approximately 220 HV which is double the hardness of the bulk material obtained from the FSP. Due to the refined layers and transition layers generated by cryogenic burnishing, the hardness became higher in the surface and subsurface layers in contrast to the hardness induced by dry burnishing, where only the surface hardness was increased.

Within the depth of 200 μm in the surface layers, the average hardness of the nine measurements (every 25 μm) has increased by 9.5%, 17.5% and 24.8% respectively, compared with the corresponding hardness of dry burnishing at the burnishing speeds of 25, 50 and 100 m/min. Herein, thermal softening plays more critical role when the burnishing temperature is increased at higher burnishing speeds. When the burnishing speed is low in dry burnishing, less thermal softening takes effect and the hardness in the subsurface is higher than the ones at high burnishing speeds. The hardness distribution is very consistent for the cryogenic burnishing, as the thermal softening effect does not play any important role.

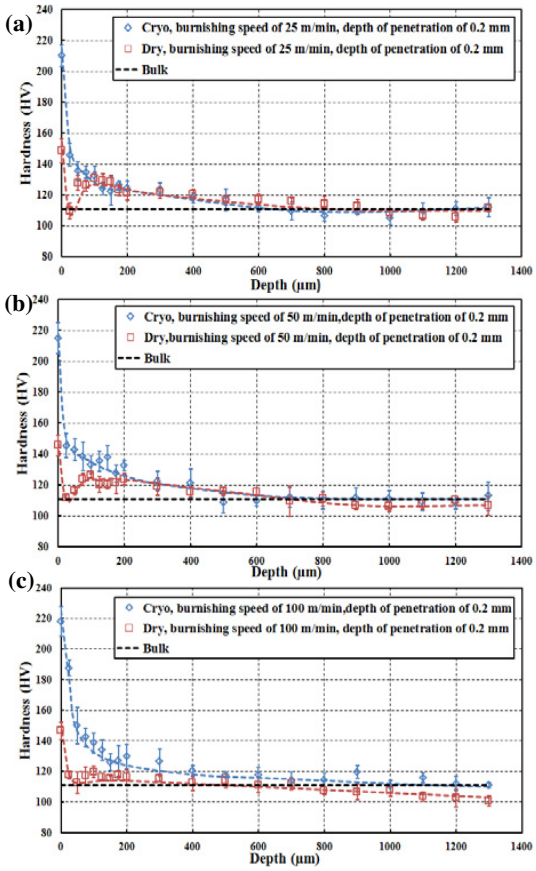

Fig. 8. Hardness distribution of *Al 7050-T7451* alloy samples from dry and cryogenic burnishing at the three different burnishing speeds: (a) 25 m/min; (b) 50 m/min; (c) 100 m/min.

4. Conclusions

Burnishing experiments were performed on *Al 7050-T7451* alloy under dry and cryogenic conditions, using liquid nitrogen as the coolant. Refined layers with nano-grains were formed in the burnished surfaces with increased hardness in the SPD layers, especially in the cryogenically burnished samples. Modified Johnson-Cook material model associated with the constitutive equations governing the flow stress change after DRX, was used to simulate the radial component of the burnishing force and the highest temperatures in dry and cryogenic burnishing. Good agreement was obtained between the simulation and experimental results. Thermal softening was observed in dry burnishing, while cryogenic burnishing shows significantly improved grain refinement and increased hardness in the burnished layer.

Acknowledgements

The authors sincerely thank Mr. Charles Arvin for his great help in conducting the burnishing experiments.

References

[1] Valiev RZ, Estrin Y, Horita Z, Langdon TG, Zehetbauer MJ and Zhu YT. Producing bulk ultrafine-grained materials by severe plastic deformation. JOM. 2006; 58(4):33-39.
[2] Estrin Y, Vinogradov A. Extreme grain refinement by severe plastic deformation: A wealth of challenging science. Acta Materialia 2013; 61: 782-817.
[3] Skalski K, Morawski A, Przybylski W. Analysis of contact elastic-plastic strains during the process of burnishing. Int. J. Mech. Sci. 1995; 37: 461-472.
[4] Grzesik W, Zak K. Modification of surface finish produced by hard turning using superfinishing and burnishing operations. Journal of Materials Processing Technology 2012; 212: 315-322.
[5] Klocke F, Backer V, Wegner H, and Zimmermann M. Finite element analysis of the roller burnishing process for fatigue resistance increase of engine components. Proceedings of the Institution of Mechanical Engineers, Part B: Journal of Engineering Manufacture 2011; 225: 2-11.
[6] Prevey PS, Cammett JT. The influence of surface enhancement by low plasticity burnishing on the corrosion fatigue performance of *AA7075-T6*. International Journal of Fatigue 2004; 26: 975-982.
[7] Pu Z, Yang S, Song GL, Dillon Jr. OW, Puleo DA and Jawahir IS. Ultrafine-grained surface layer on *Mg-Al-Zn* alloy produced by cryogenic burnishing for enhanced corrosion resistance. Scripta Materialia 2011; 65: 520-523.
[8] Yang S, Dillon Jr. OW, Puleo DA, Jawahir IS. Effect of cryogenic burnishing on surface integrity modifications of *Co-Cr-Mo* biomedical alloy. J Biomed Mater Res Part B 2013; 101B:139-152.
[9] Yang S. Cryogenic burnishing of *Co-Cr-Mo* biomedical alloy for enhanced surface integrity and improved wear performance. Doctoral Dissertation, University of Kentucky, 2012.
[10] Alcoa. Discover Aluminum Again. Discover Alcoa's Cost-effective and Proven New Technology 2012.
[11] Zhao Z, Hong SY. Cooling strategies for cryogenic machining from a materials viewpoint. J. Mater. Eng. Perform. 1992, 1 (5):669-678.
[12] Yang S, Puleo DA, Dillon Jr. OW, Jawahir IS. Surface layer modifications in *Co-Cr-Mo* biomedical alloy from cryogenic burnishing. Procedia Engineering 2011; 19: 383-388.
[13] Hamilton C, Sommers A, Dymek S. A thermal model of friction stir welding applied to Sc-modified *Al–Zn–Mg–Cu* alloy extrusions. International Journal of Machine Tools & Manufacture 2009; 49: 230-238.
[14] Johnson GR, Cook WH. A constitutive model and data for metals subjected to large strains, high rates and high temperatures. In Proceedings of the Seventh International Symposium on Ballistics, The Netherlands: The Hague, 1983, 541-547.
[15] Wu. B, Li MQ, Ma DW. The flow stress behavior and constitutive equations in isothermal compression of *7050* aluminum alloy. Materials Science and Engineering A 2012; 542: 79-87.
[16] Sarkar A, Chakravartty JK, Paul B, Suri, AK. Kinetics of dynamic recrystallization in cobalt: A study using the Avrami relation. Physical Status Solidi a-Applications and Mat. Science 2011; 208 (4): 814-818.
[17] Wang ZQ, Li JF, Sun J, Jiang F, Zhou J. Flow stress determination of aluminum alloy *7050-T7451* using inverse analysis method. Key Engineering Materials 2010; 431-432: 174-177.
[18] Wang FZ, Sun J, Sun PQ, Zhou J. Finite element model and analysis for micro-cutting of aluminum alloy *7050-T7451*. International Journal of Materials and Mechanics Engineering 2012; 566: 650-653.
[19] Fu XL, Wang H, Wan Y, Wang XQ. Material constitutive model in machining *7050-T7451* by orthogonal machining experiments. Advanced Materials Research 2010; 97-101:713-716.
[20] Wen C, Mudawar I. Emissivity characteristics of roughened aluminum alloy surfaces and assessment of multispectral radiation thermometry (MRT) emissivity models. International Journal of Heat and Mass Transfer 2004; 47: 3591-3605.
[21] Strasik M, Hull JR, Mittleider JA, Gonder JF, Johnson PE, McCrary KE, McIver CR. An overview of Boeing flywheel energy storage systems with high-temperature superconducting bearings. Supercond. Sci. Technol 2010; 23: 034021 (5pp).
[22] Tang ZT, Liu ZQ, Pan YZ, Wan Y, Ai X. The influence of tool flank wear on residual stresses induced by milling aluminum alloy. Journal of Materials Processing Technology 2009; 209: 4502-4508.
[23] Sandstrom DR, Hodowany JN. Modeling the physics of metal cutting in high-speed machining. Machining Science and Technology 1998; 2:343-353.
[24] Zhou J, Li J, Sun J. Finite element analysis of micro-cutting aluminum *7050-T7451* with the tool edge radius considered. Key Engineering Materials 2010; 443: 663-668.